Sensitivity Analysis of a 3D Convective Storm: Implications for Variational Data Assimilation and Forecast Error

SEON KI PARK* AND KELVIN K. DROEGEMEIER

Center for Analysis and Prediction of Storms and School of Meteorology, University of Oklahoma, Norman, Oklahoma

(Manuscript received 27 July 1998, in final form 23 February 1999)

ABSTRACT

In this study a nonhydrostatic 3D cloud model, along with an automatic differentiation tool, is used to investigate the sensitivity of a supercell storm to prescribed errors (perturbations) in the water vapor field. The evolution of individual storms is strongly influenced by these perturbations, though the specific impact depends upon their location in time and space. Generally, perturbations in the rain region above cloud base have the largest impact on storm dynamics, especially for subsequent storms, while perturbations in the ambient environment above cloud base influence mostly the main storm. Although perturbations in the subcloud layer have a relatively small impact on upper-level storm structure, they do impact the low-level structure, especially during the period immediately following insertion.

Sensitivities are also examined in the context of variational data assimilation and forecast error. For perturbations added inside the active storm, the cost function, which is prescribed to measure the discrepancy between forecast and observations for all variables over time and space, is found to be most sensitive to temperature, followed by pressure and water vapor. This implies that the quality of variational data assimilation can be affected by the inaccuracy of observing or retrieving those quantities. It is also noted that, at least for the case studied here, the pressure field has the largest influence on forecast error immediately after the errors are inserted, while the temperature field does so over a longer time period.

1. Introduction

The dynamical evolution of numerically simulated convective storms is dependent upon a number of factors, including physical parameterizations, numerical schemes and related computational parameters, and initial and boundary conditions. Many strategies are available to assess this dependence or sensitivity. The deterministic approach, which employs both the tangent linear and adjoint of the original nonlinear model (e.g., Worley et al. 1987; Errico and Vukicevic 1992; Park and Droegemeier 1999), can provide a wealth of sensitivity information at very low cost compared to traditional brute force (e.g., Monte Carlo) methods that involve making numerous simulations with the full numerical model and performing various types of statistical analysis on the output (e.g., Leith 1974; Seigneur et al. 1981).

In the deterministic approach, one develops a set of differential sensitivity equations to express the gradient of the solution vector with respect to input parameters (Worley et al. 1987). Sensitivity coefficients, defined as the first-order partial derivatives in the Taylor expansion (Dunker 1981), are then computed exactly by solving the differential equations—either tangent linear model (TLM) or adjoint model (ADJM)—using a particular nonlinear solution as a basic state (e.g., Errico and Vukicevic 1992; Bischof et al. 1996b; Park et al. 1996; Park and Droegemeier 1999). In this regard, the sensitivity is defined as the gradient (i.e., the first-order derivative) of the model response with respect to any input parameter (Ronen 1988). Sensitivity is defined in a more general way in Zou et al. (1993a).

Automatic differentiation (AD) tools, which apply the chain rule systematically to elementary operations or functions to generate derivative codes (TLM and/or ADJM) of nonlinear models (Bischof and Dilley 1995), can be used to compute the gradients efficiently and accurately. Additionally, AD tools are powerful for use in four-dimensional variational data assimilation (4D-Var), where nonlinear optimization requires gradient information.

In meteorology, the ADJM has been used effectively in both sensitivity analysis (e.g., Errico and Vukicevic

* Current affiliation: Department of Meteorology, University of Maryland, College Park, Maryland.

Corresponding author address: Dr. Seon Ki Park, Department of Meteorology, University of Maryland, 3433 Computer and Space Science Building, College Park, MD 20742.
E-mail: skpark@atmos.umd.edu

1992; Zou et al. 1993a) and variational data assimilation (e.g., Lewis and Derber 1985; Chao and Chang 1992; Zou et al. 1993c; Wang et al. 1997). Although AD tools exist for generating the ADJM [e.g., Odyssée, Rostaing et al. (1993); TAMC, Giering (1997)], they are still routinely generated by hand, particularly for complex 3D models. A compilation of AD tools currently available can be found in Bischof and Dilley (1995).

In our companion paper (Park and Droegemeier 1999), we applied a general-purpose AD tool [ADIFOR—Automatic Differentiation of FORTRAN; Bischof et al. (1996a)] to a 1D cloud model to investigate the sensitivity of moist convective dynamics to selected input parameters. Although some concern exists regarding the validity of the linear approximation in terms of the *discontinuities* and *strong nonlinearity* inherent in model physical processes, the TLM has been shown to be valid for 40–50 min in moist convective dynamics (Park and Droegemeier 1997a).

In the present study we extend the AD procedure to a supercell storm using a nonhydrostatic 3D cloud model known as the Advanced Regional Prediction System (ARPS; Xue et al. 1995). More specifically, we use ADIFOR to generate a sensitivity-enhanced ARPS (hereafter SE-ARPS) code capable of providing derivatives of all model output variables and related diagnostic (derived) parameters [i.e., termed dependent variables (DVs)] as a function of specified control parameters, including initial and boundary conditions as well as physical and computational constants [i.e., termed independent variables (IVs)]. In this manner, we obtain *exact* derivative information to establish physical/dynamical cause and effect between changes in input and changes in output.

The ARPS is a large and complex model consisting of more than 250 subroutines; developing its adjoint code by hand is a tedious, time-consuming, and error-prone process. Because the ARPS complies with the FORTRAN 77 standard, as required by ADIFOR, the SE-ARPS code was generated very quickly and easily. The ADIFOR also differentiates the on–off switches for microphysical processes, which are mostly represented by ''if–then'' statements, in a similar way as described in Zou et al. (1993c). (The TLM validation of the SE-ARPS will appear in section 5.)

Recently, the TLM and ADJM of ARPS have been developed manually but not for all physics packages. An adiabatic version of the ARPS has been employed to develop the corresponding TLM for sensitivity analysis (Wang et al. 1995), and the associated ADJM for 4D-Var (Wang et al. 1997). Although Park and Droegemeier (1997b) applied the ADJM of ARPS with warm-rain microphysics to 4D-Var, to our knowledge, no AD tool has been applied to a 3D compressible cloud-scale model until now.

The major goal of this study is to investigate, using the ADIFOR-generated derivative code of ARPS (SE-ARPS), the sensitivity of a numerically simulated convective storm to changes in input parameters, especially in moisture. Moisture is an essential factor in storm dynamics and morphology. The low-level moisture controls the timing and persistence of clouds (Hong et al. 1995). Crook (1996) illustrates that, for cases in which convection is well developed, the storm strength (maximum vertical velocity) is more sensitive to the typical observational variability in moisture (1 g kg^{-1}) than in temperature (1°C). In addition, both the strength and timing of the surface outflow are highly sensitive to moisture changes due to dry air intrusion in the lower or midddle troposphere (Gilmore and Wicker 1996).

Krumm (1954) indicates that precision in low relative humidity data is an important issue in forecasting and detection of downdraft environment. However, most contemporary radiosonde instruments show extremely low performance in measuring relative humidity at cold and dry regions (Pratt 1985; Elliott and Gaffen 1991). Relative humidity reports are usually biased negatively, by several percent (lower troposphere) to as much as about 20% (upper troposphere), as a result of thermal lag and warming by sunlight (Pratt 1985).

These studies demonstrated the possibility of errors in current observations of water vapor. In the context of storm-scale numerical prediction (e.g., Droegemeier et al. 1996; Xue et al. 1996; Hong et al. 1995; Weygandt et al. 1990), it may provide the major difficulty in accurate forecast of deep convective storms. Thus, an understanding of sensitivity due to perturbations in water vapor is essential.

Section 2 describes the method used to compute various sensitivities, and section 3 explains the basic features of the ARPS and parameters used in this study. Section 4 shows the evolution of the convective storm from the control simulation, and in section 5 we verify the SE-ARPS by examining the validity of the tangent linear approximation against the corresponding nonlinear perturbation (NLP—i.e., difference between perturbation and control runs) solutions obtained by varying the perturbation size and insertion times. The basic assumption in this approach is that, according to the Taylor approximation, the TLM solutions should approach the NLP fields as the perturbation size decreases.

In section 6, we evaluate the sensitivity of the same storm to the water vapor field in four separate regions: inside the storm, in the ambient environment above cloud base, and in the updraft and downdraft regions below cloud base. In section 7, we assess the relative importance among model variables in the context of variational data assimilation and forecast error. A summary and discussion are provided in section 8.

2. Methodology—Sensitivity to perturbations

The ADIFOR is a forward-mode-based automatic differentiation tool. Thus it generates a tangent linear code that is designed to compute sensitivities of all DVs with respect to all IVs for a single run. A single run of the

ADIFOR-generated derivative code is equivalent to as many tangent linear model runs as the number of IVs, though the ADIFOR can save computing time through a hybrid technique (Bischof et al. 1996a).

In the context of 3D models, the number of IVs (and degrees of freedom) is potentially very large, thus inhibiting the computation of sensitivity information using an ADIFOR-generated code due to computer memory constraints. We therefore compute sensitivities with respect to *perturbations* inserted in model variables rather than to the grid variables themselves. That is, by introducing an artificial perturbation parameter, e, into the original forward model (ARPS), ADIFOR can generate a sensitivity code that regards e as one of the IVs (Bischof et al. 1996b).

Consider, for example, the water vapor field (Q_v). If we perturb it by a factor e (the form of which is yet to be specified),

$$Q_v(x, y, z, t; e) = (1 + e)Q_v(x, y, z, t), \qquad (1)$$

then any quantity P that is influenced by the water vapor field implicitly depends upon e. Expanding $P(e)$ in a Taylor series about the reference state [$P(e = 0)$] and retaining only the first-order term, we obtain an approximation of the sensitivity of P with respect to e:

$$S(x, y, z, t; e) = \left.\frac{\partial P(x, y, z, t; e)}{\partial e}\right|_{e=0}. \qquad (2)$$

In our example, S can be interpreted as the sensitivity of P to a *uniform relative change* in the water vapor field. We have modified the ARPS to include e as an input parameter, as shown in Eq. (1) and have applied ADIFOR to differentiate this code with respect to e.

Because e is nondimensional, we can easily define the relative sensitivity coefficient [RSC; see Park and Droegemeier (1999)] as

$$\mathrm{RSC} = \frac{\left(\frac{\partial P}{\partial e}\right)}{\left(\frac{P}{e}\right)}. \qquad (3)$$

This formulation is useful for comparing the relative importance among sensitivities computed for different variables (i.e., the percentage change in P due to a 1% change in e).

With the formulation in (1), we consider only bias error. Although bias does not account for the whole sprectrum of possible errors and thus may not represent effective nonlinear interactions of errors, it is quite important in observation and retrieval (e.g., Pratt 1985). Also, Eq. (1) can be easily extended to include other types of errors, for example, random (Bischof et al. 1996b). Although the way the error is prescribed in (1) may not include absolute errors (i.e., it is limited to bias and random type errors), it is the fractional change in water vapor rather than absolute change that is important (Shine and Sinha 1991).

We limit our experiments here to variations in initial conditions only. The sensitivity of storm evolution to perturbations in boundary conditions is, by itself, a very important issue in numerical weather prediction. However, since the current effort is a first step toward assessing sensitivities in a 3D convective storm using the AD technique, we limit the scope of our study appropriately.

3. Model description

Our experiments are performed using the sensitivity-enhanced code generated from version 4.0 of ARPS (Xue et al. 1995), which is a three-dimensional, fully compressible, and nonhydrostatic meso- and storm-scale model. The prognostic variables, solved on the Arakawa C grid (Arakawa and Lamb 1977), include Cartesian velocity components (u, v, and w), perturbations of potential temperature (θ') and pressure (p'), mixing ratios of water vapor (Q_v), cloud water (Q_c) and rainwater (Q_r), and turbulent kinetic energy. (Ice processes are neglected in our study.) The advective modes are computed on big time steps with the leapfrog scheme and second-order centered space differencing, whereas the acoustic modes are integrated on small time steps with an implicit scheme. We operate the model in a very simple mode using only Kessler explicit warm-rain microphysics (Kessler 1969). An extensive description of the model can be found in Xue et al. (1995).

The model configuration for our experiments is summarized in Table 1. The computational domain consists of 53 × 53 points in the horizontal with a grid size of 1 km. In the vertical, a stretched grid system is employed using 35 levels with a resolution of 150 m near the ground and 850 m at the top of the domain (the model top is at 16 km). The stretching function is a hyperbolic tangent, resulting in 10 grid points below 2 km. The model is run for 140 min using a big time step of 6 s and a small time step of 1 s. The boundary conditions include wave radiation on the lateral boundaries (Klemp and Wilhelmson 1978) and rigid, free-slip plates at the top and bottom.

4. Control simulation

The simulation to verify the computation of derivatives by ADIFOR is made using the Droegemeier et al. (1993) HALF4 (supercell) hodograph and thermodynamic sounding, the latter of which has a surface mixing ratio of 15 g kg^{-1}. The wind profile consists of a semicircular hodograph arc of 10 m s^{-1} radius that turns clockwise over the lowest 4 km starting with easterly winds at the surface. The (westerly) wind is constant with height above 4 km at a speed of 10 m s^{-1}. Convection is initiated by a 4-K thermal perturbation placed in the boundary layer.

TABLE 1. ARPS model parameters for control simulation.

Definition	Parameter	Value
Physical domain	$XL \times YL \times ZH$	50 km × 50 km × 16 km
Computational domain	$nx \times ny \times nz$	53 × 53 × 35
Horizontal grid spacing	dx, dy	1 km
Vertical grid spacing (stretching)	$dzmin$	150 m
Big time step	$dtbig$	6.0 s
Small time step	$dtsml$	1.0 s
Second-order vertical mixing coef	$cfcm2v$	4.0×10^{-4} s^{-1}
Fourth-order horizontal mixing coef	$cfcm4h$	1.0×10^{-3} s^{-1}
Divergence damping coef	$divdmpnd$	0.05
Rayleigh damping coef	$cfrdmp$	0.00333
Rayleigh sponge bottom	$zbrdmp$	12 km
Thermal perturbation	θ_0	4 K
Initial bubble center location	(x_c, y_c, z_c)	(10 km, 27 km, 1 km)
Initial bubble radii	(x_r, y_r, z_r)	(5 km, 5 km, 1 km)

As illustrated by the domain-maximum updraft in Fig. 1, the simulated supercell develops rapidly during the first 30 min and becomes quasi-steady thereafter with a sustained updraft of around 47 m s^{-1}. In Fig. 2, the surface outflow boundary and vertical velocity at 4 km are depicted at t = 30, 50, 90, 110, 120, and 140 min. The storm moves to the west initially and then turns northeastward as it grows in vertical extent, forming a surface cold pool (t = 30 min; Fig. 2a).

Another storm is triggered by convergence along the northern gust front (t = 40 min; not shown). Also, as the northeast part of the gust front intensifies, a new cell develops along it (t = 50 min; Fig. 2b), constituting three distinct cells. As the northern part of the gust front moves northward out of the model domain by 60 min, the two northern storms decay and other weak secondary storms form near the northern lateral boundary (t = 90 min; Fig. 2c). The dominant storm thereafter is an isolated supercell that travels southeastward along the leading edge of the expanding cold pool.

A secondary storm develops northeast of the main storm after 100 min, merging into the main storm by 140 min (Figs. 2d–f). A prominent kink in the surface outflow develops after 130 min, which is evidence of low-level mesocyclone development (see Droegemeier et al. 1993 for details).

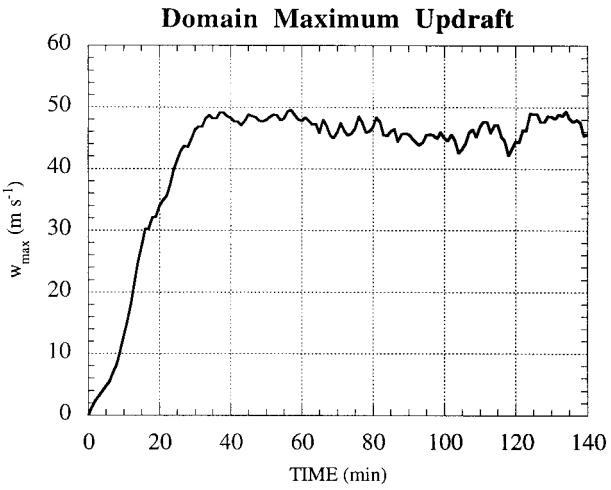

FIG. 1. Domain-maximum updraft speed for the control simulation (in m s^{-1}).

5. Validation of TLM solutions using SE-ARPS

Before we proceed to the sensitivity computation, the TLM solutions computed by the ADIFOR-generated code (SE-ARPS), which describe the linear evolution of perturbations, are validated by comparison against the NLP fields, that is, the difference fields computed between the nonlinear control run and another nonlinear run, whose initial state is slightly perturbed from it using the same perturbation as in the TLM.

Note that the SE-ARPS handles the on–off switches as most ''classic'' TLMs do (e.g., Zou et al. 1993c), which do not consider the variation of switch time. However, Park and Droegemeier (1997a) showed that the TLM validity due to the switching time variation is affected significantly only when a ''large'' perturbation is given. Since our TLM solutions are computed for reasonably small perturbations, they may not cause a serious problem.

Figure 3 shows the TLM and NLP fields of vertical velocity (w) at 45 min for a 1% bias perturbation in water vapor (Q_v) over the entire model domain except for the lateral, top, and bottom boundaries. Shown are the x–z planes where the domain maximum of w occurs. The TLM fields predict that the perturbation introduced in Q_v at the initial time induces positive perturbations in w from the middle to upper levels near the southern edge of the main storm, with maximum perturbations near 12 km. The TLM and NLP fields agree quite well in both magnitude and location.

After about 55 min (Fig. 4), the solutions begin to diverge. Although the locations match reasonably well, the magnitude differences are significant. That is, in reality, the perturbations and (time evolving) nonlinear

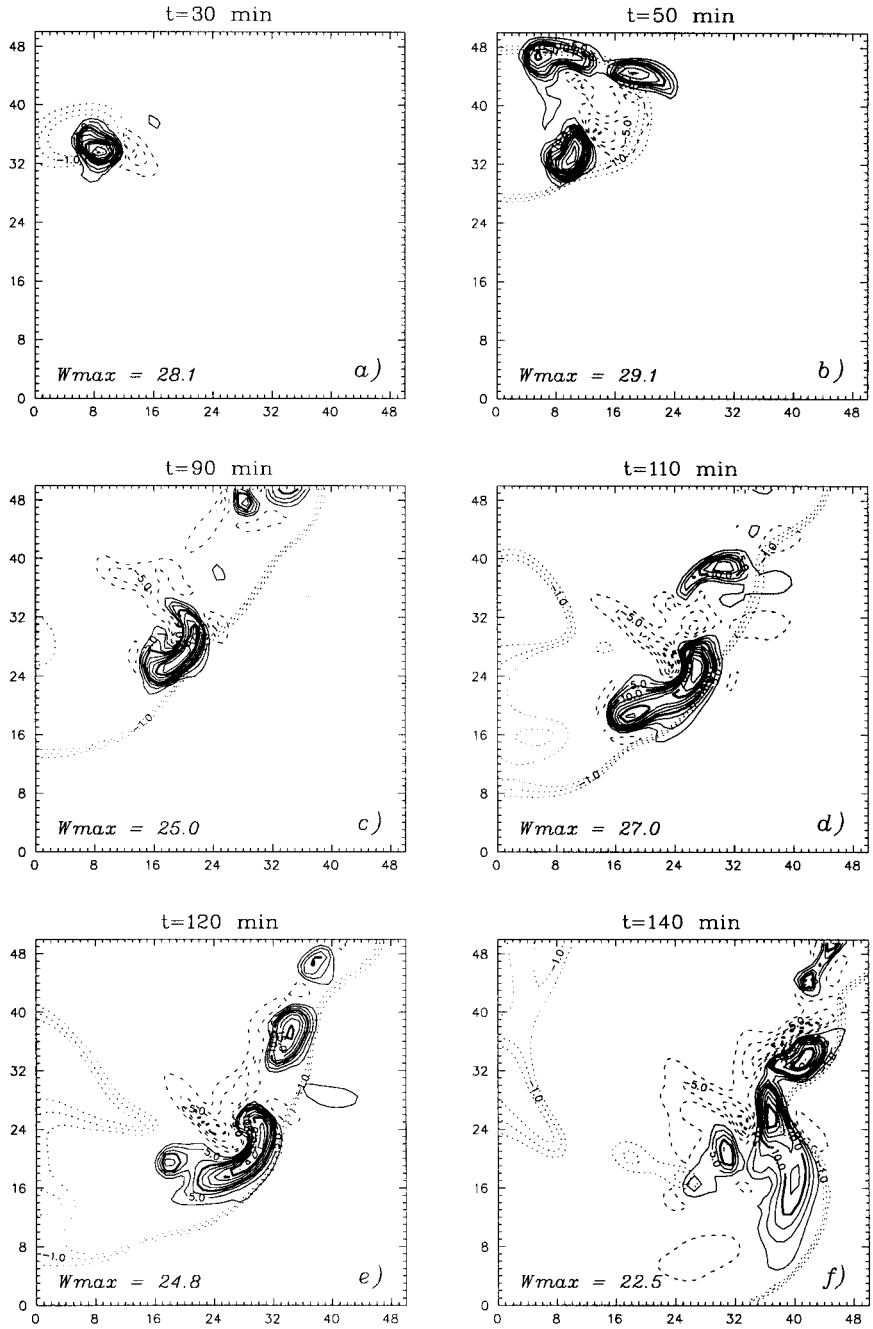

FIG. 2. Control simulation: vertical velocity at 4 km (positive in solid and negative in dashed lines at the interval of 2.5 m s^{-1}) and perturbation potential temperature at surface (dotted lines with contours larger than −2.0 K at the interval of 0.5 K) at (a) 30, (b) 50, (c) 90, (d) 110, (e) 120, and (f) 140 min.

base state interact to a significant extent, and the absence of this interaction in the TLM leads to erroneous results.

Based on the TLM validity demonstrated here for a 1% perturbation in Q_v, we investigate in the following subsections variations in TLM validity for different perturbation sizes and insertion times. The results are discussed in terms of selected statistical parameters such as the correlation coefficient (COR) between the TLM and NLP and the nonlinearity coefficient (NLC), the latter of which is expressed as [see Eq. (10) in Park and Droegemeier (1997a)]

$$\mathrm{NLC} = \frac{\|\mathrm{NLP} - \mathrm{TLM}\|}{\|\mathrm{TLM}\|} \tag{4}$$

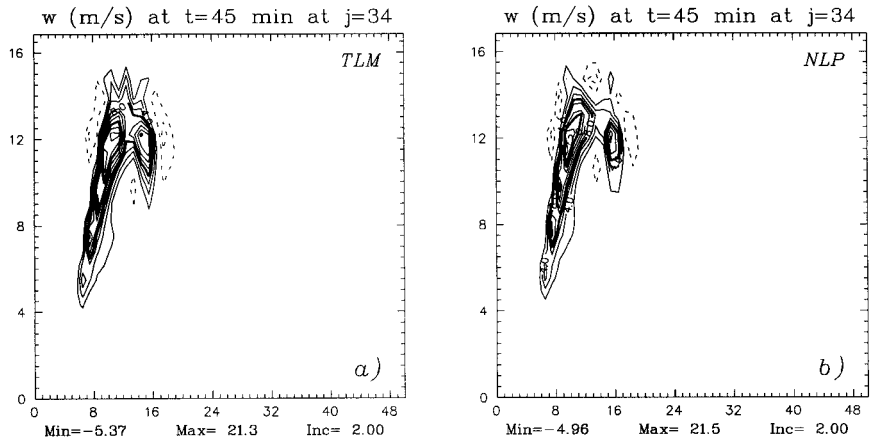

FIG. 3. The x–z slices (at $j = 34$) of (a) tangent linear perturbation and (b) nonlinear perturbation in w at $t = 45$ min for a 1% perturbation in Q_v (in m s^{-1}).

and which measures the relative importance of the first-order (linear) and higher-order (nonlinear) terms in the Taylor series.

a. Variation in perturbation magnitude

As illustrated in the 1D cloud experiments of Park and Droegemeier (1997a), TLM validity depends upon the amplitude of specified perturbation. To examine this dependence in our 3D storm, we repeat the above experiment using a smaller perturbation (0.1%) and run the SE-ARPS for 140 min.

In Fig. 5, the COR and NLC are shown for the w fields for the two perturbation experiments (0.1% and 1%) every 5 min. The time over which the correlation (nonlinearity) stays high (low) becomes longer as the perturbation size decreases. Thus, as expected, a weaker perturbation improves the validity of the TLM. For a 0.1% perturbation, the TLM is valid up to 100 min, after which the correlation (nonlinearity) shows a rapid decrease (increase). Our results also demonstrate that, from the definition of the NLC in Eq. (4), the correlation between the linear and nonlinear perturbation fields starts to drop noticeably when the magnitude of the higher-order terms reaches about half the magnitude of the first-order term.

It should be noted that errors in humidity measurement typically range from several percent (lower troposphere) to about 20% (upper troposphere) (Pratt 1985). Using a 10% perturbation in the initial Q_v field (not shown), the TLM was valid up to 30 min in a marginal sense (NLC > 1 but stays at low values, e.g., less than 1.2) but around 10 min in a strict sense (NLC < 1). This implies that, for perturbations typical of observational errors or retrievals in this particular supercell simulation with full physics, accurate sensitivity (gradient) information using the TLM/ADJM can be obtained for only about 10–30 min.

b. Variation in perturbation insertion time

Another important issue is the variation in TLM validity for different perturbation insertion times. Because

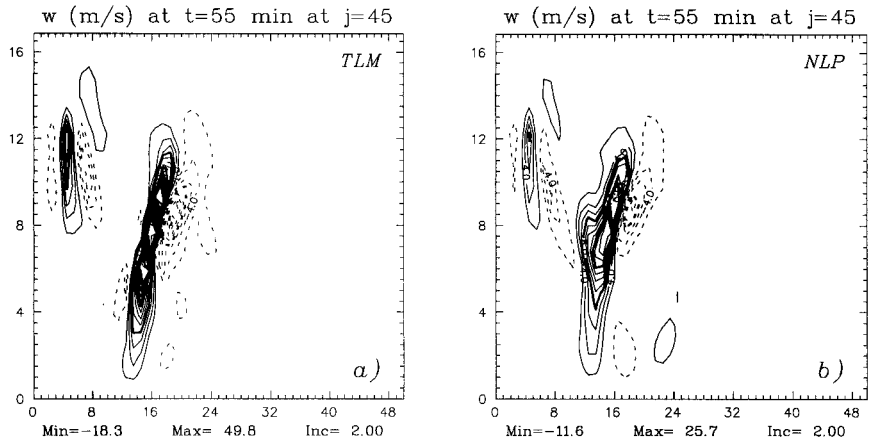

FIG. 4. Same as in Fig. 3 except for $j = 45$ and $t = 55$ min (in m s^{-1}).

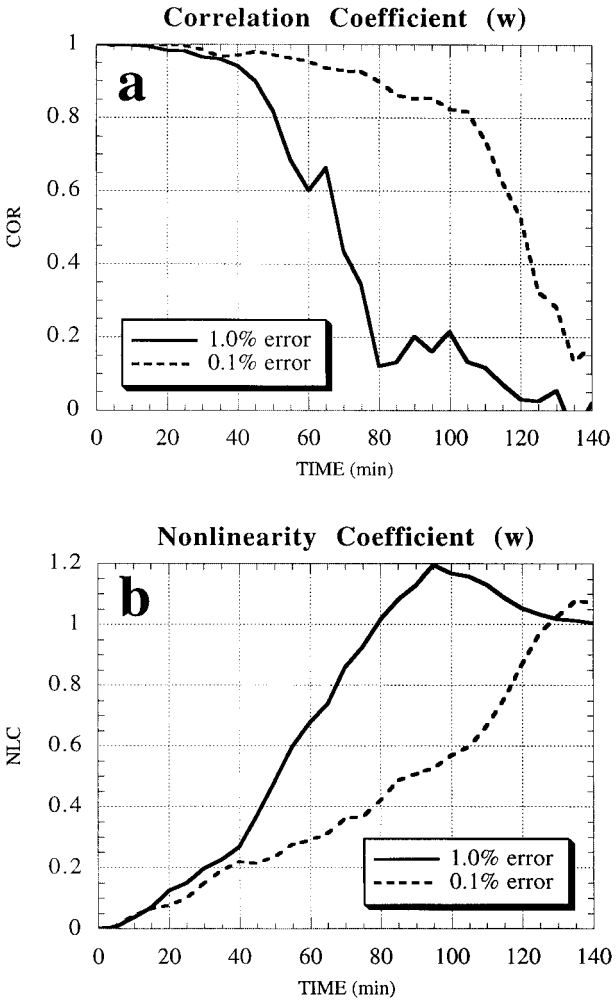

FIG. 5. (a) Correlation coefficient between the linear and nonlinear perturbation fields and (b) nonlinearity coefficient of vertical velocity for 1% and 0.1% perturbations in water vapor, respectively.

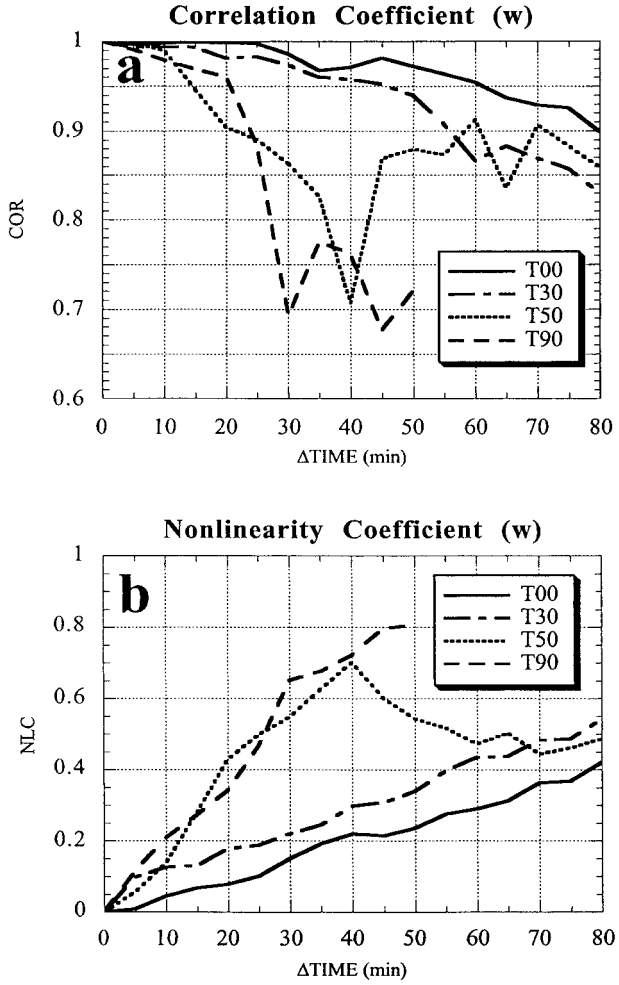

FIG. 6. Same as in Fig. 5 except for a 0.1% perturbation in water vapor inserted at $t = 0$, 30, 50, and 90 min, respectively. The abscissa (ΔTIME) is the elapsed time from perturbation insertion.

each stage of storm evolution is somewhat different in the relative importance of physical processes, most of which are inherently discontinuous and strongly nonlinear, the validity of the linear approximation may vary significantly for identical perturbations inserted at different times.

We have performed TLM validity experiments for the following perturbation insertion times using a 0.1% bias in water vapor, as before: $t_0 = 0$ min (case T00, which was discussed above), 30 min (case T30), 50 min (case T50), and 90 min (case T90). Case T30 has only a single cell storm in its developing stage, while case T50 includes three cells (see Fig. 2). In case T90, the storm at the southern part of the outflow evolves into a supercell with a typical ''lima bean'' shape in rainwater field.

Figure 6 shows the COR and NLC of vertical velocity for perturbations at different insertion times. Note that the abscissa is the time interval (Δt) from the times of perturbation insertion. For example, $\Delta t = 40$ min represents $t = 70$ min for case T30, $t = 90$ min for case T50, and $t = 130$ min for case T90. A statistical analysis has been performed below $z = 12$ km (the bottom of the Rayleigh sponge).

In all cases, for the 0.1% perturbation, the CORs seem to be fairly high and the NLCs are quite small (Figs. 6a and 6b). Similar to the experiment in section 5a, changes in correlation patterns are associated with changes in nonlinearity. Notably, the TLM validity shows different characteristics for different perturbation insertion times. Some interesting features are the following. 1) The statistical parameters change abruptly after perturbations are inserted for cases T50 and T90, while they change slowly throughout the simulation for case T00 and T30. Even though cases T30 and T90 initially contain only a single cell in the model domain, the patterns in the CORs and NLCs are very different. 2) The NLC in case T50 decreases after $\Delta t = 40$ min,

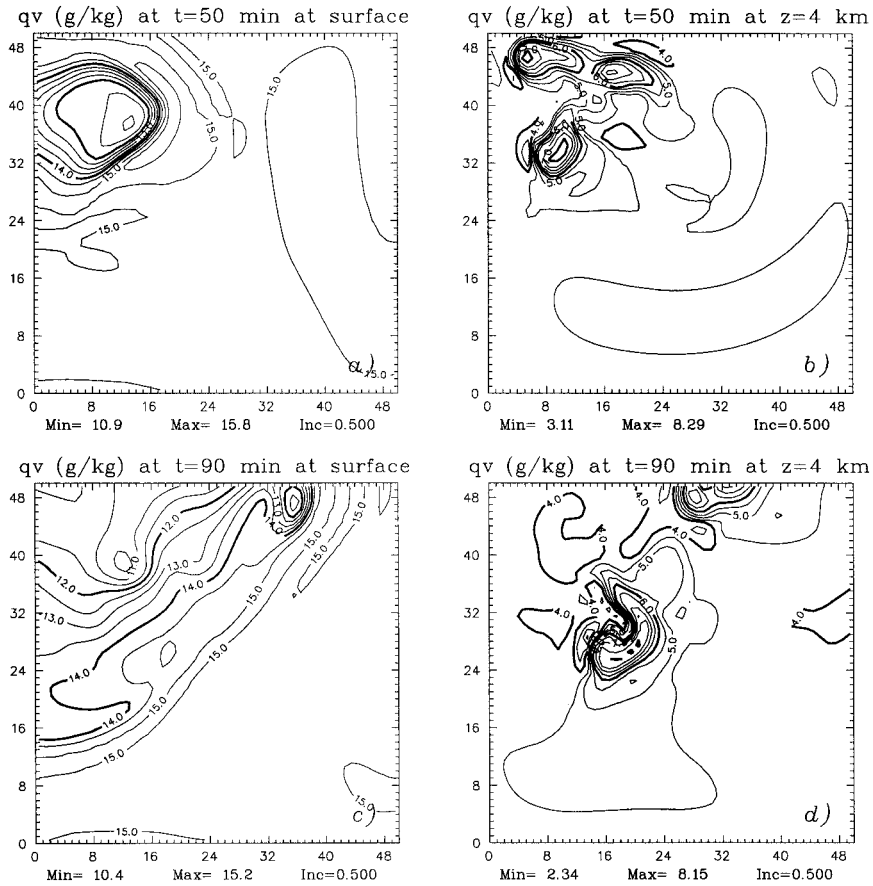

FIG. 7. Water vapor for $t = 50$ min (T50; upper panel) at (a) the surface and (b) 4 km and for $t = 90$ min (T90; lower panel) at (c) the surface and (d) 4 km (in g kg^{-1}).

while the NLCs for all other cases continuously increase. The bases for this behavior are as follows.

Since the convective storm in our case develops from an idealized thermal bubble in the lower atmosphere, the system experiences transience before it forms a stable convective cell (quasi-equilibrium state). As shown in Fig. 1, the vertical velocity increases rapidly during the first 30 min and then reaches an equilibrium state. During this transition period, due to a relatively weak influence by physical processes, the nonlinearity does not increase significantly; thus, both the T00 and T30 cases show reasonable TLM validity. After the transition period, as seen in Figs. 1 and 2, the major convective cell evolves into a supercell storm, while others move out of the domain with the expansion of the surface outflow. Although supercell storms show rather stable behavior, they include very complex physical and dynamical processes, which can seriously affect TLM validity.

The difference in the areas occupied by storms at the perturbation insertion times may also affect TLM validity. For instance, areas of cloud and rainwater, which are associated with on–off switches, are much larger in cases T50 and T90 than in T30. Although the magnitude of the updrafts at the time of perturbation insertion is similar for these cases (see Fig. 1), the region occupied by the updraft is much different. A larger updraft volume can change the involvement of physical processes, especially condensation.

Another possibility includes differences in the amount of nonlinearity present in the system when the perturbations are inserted. For example, for the perturbation inserted at $t = 0$ (i.e., case T00), the NLC increases steadily with time. Thus, when small perturbations are inserted early enough, the existing nonlinearity may be sufficiently weak so that the chance for strong nonlinear interaction between the inserted perturbations and other variables is reduced, thus extending TLM validity.

In addition, we note that the absolute perturbation for a 0.1% *relative* perturbation is different for each case due to the different distribution of water vapor (Q_v) at any given time in the control run. Figure 7 shows the distribution of Q_v at the surface and at 4 km at $t = 50$ and 90 min. The largest values are at low levels, and although the maximum value of Q_v in T50 is larger than in T90, Q_v in the latter is distributed over a much broader area (Figs. 7a and 7c). At higher levels, though, the Q_v distributions are similar in area for both cases, and the

magnitude of the perturbations are small compared to those at the surface (Figs. 7b and 7d). Therefore, the absolute perturbation magnitude in T50 might be smaller and thus more tolerable for the tangent linear approximation than in T90.

Finally, differences in storm structure may play a role in error growth. The T50 case starts with three equally sized storm cells in the domain; passes through a single supercell within the first 40 min, when the NLC starts to decrease; and then ends up with one major supercell and two secondary storms. On the other hand, T90 starts with a single supercell and ends up similar to T50. Although the absolute perturbation magnitude is small in T50, the NLC of T50 evolves in a similar manner to that of T90 shortly after perturbation insertion due to the complex three-cell structure at the error insertion time.

6. Sensitivity results

Having examined the TLM under various sorts of perturbations, we now investigate the effect on storm dynamics of perturbations in the water vapor (Q_v) field. We introduce four perturbation equations following Eq. (1) for four different regions in the model: (e_1) inside the storm ($Q_r > 1.0 \times 10^{-4}$ g g^{-1}) above cloud base, (e_2) in the ambient environment ($Q_r < 1.0 \times 10^{-4}$ g g^{-1}) above cloud base, (e_3) in the inflow/updraft region (including $w = 0$) in the subcloud layer, and (e_4) in the downdraft region in the subcloud layer. Note that the perturbation regions are divided in terms of Q_r, and the pattern of perturbed quantity (Q_v) does not generally match that of Q_r. For example, the maximum Q_v at 50 min and $z = 4$ km (see Fig. 7b) is located outside the storm near the storm boundary (e_2 region; Q_r is not shown).

Using these four perturbations (e_1–e_4), we run the SEARPS starting at 50 min (T50) and 90 min (T90) and ending at 140 min; that is, the effect of the perturbation begins when the storm is in its developing and mature stages, respectively. Among the many available results, we focus on the sensitivity of vertical velocity, surface rainfall, and accumulated rainfall.

The cloud base at $t = 50$ min is around 640 m, and four model levels are involved in the subcloud layer (excluding the bottom boundary). At $t = 90$ min, cloud base is located at 485 m with three levels in the subcloud layer. The numbers of grid points involved in the perturbed regions are 8280 for e_1, 61 720 for e_2, 5972 for e_3, and 4028 for e_4, in case T50; and 14 878 for e_1, 57 622 for e_2, 5333 for e_3, and 2167 for e_4, in case T90.

a. Sensitivity of vertical velocity

Figure 8 shows time series of the domain-maximum sensitivities of w {i.e., $[\partial w(t > t_i)/\partial e(t_i)]_{\max}$, where t_i is the perturbation insertion time} at 5-min intervals. For

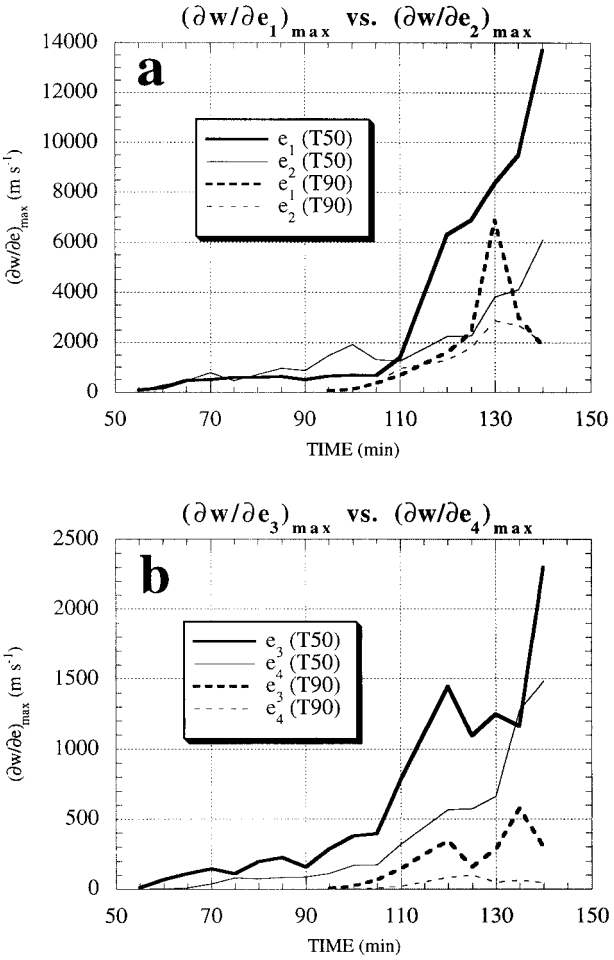

FIG. 8. Domain-maximum sensitivity of w with respect to perturbations of (a) e_1 and e_2, and (b) e_3 and e_4 (in m s^{-1}). Solid lines are for case T50 and dashed lines for case T90.

both T50 and T90, the sensitivities of w to the e_1 and e_2 perturbations (Fig. 8a) are much larger than those to e_3 and e_4 (Fig. 8b). (Note the difference in the ordinates.) The heights where these maximum sensitivities occur are generally between 8 and 14 km (levels 24–31).

Overall, the e_1 perturbation brings about the largest change in w throughout the sensitivity period, except during the early stages when the e_2 perturbation dominates. It should be noted that the sensitivity values shown here are defined as the change in w for a 100% error in Q_v. For example, the maximum sensitivity of w (13 700 m s^{-1}) with respect to the e_1 perturbation (case T50 at $t = 140$ min) implies that w will increase by 13.7 m s^{-1} at $t = 140$ min when only a 0.1% error is present in the in-storm vapor field at $t = 50$ min. Our results suggest that, even with very small errors (as low as 0.1%) in measured or retrieved water vapor, the maximum change in vertical velocity predicted by a numerical model can be significant.

The increased moisture above the boundary layer increases saturation/supersaturations, and thus conden-

sation in the high Q_v area, and destabilizes the atmosphere due to the increase in the equivalent potential temperature. Further, the additional latent heat release due to increased condensation creates additional buoyancy, which in turn leads to stronger updrafts. This effect will be greater when the moisture increase occurs inside the storm. The larger sensitivity to the e_2 perturbation during the early period may partly result from the larger number of grid points initially perturbed: e_1 is only about 13% of that for e_2 in T50 and 25% in T90. The perturbations added to this larger volume outside the storm affect w sooner than the perturbations in a much smaller volume inside the storm. This is also evident in case T90, although it occurs over a shorter time period. In addition, the region of high Q_v also occurs outside the main storm near the storm boundary. Thus increasing Q_v in the e_2 region, especially in the area of high Q_v, can result in supersaturations or saturation in regions that were previously close to but below saturation and thus condensation and eventually stronger updraft.

It is also apparent that the impact of the perturbations is highly dependent upon storm structure at the time the perturbations are introduced. For example, for the same time interval after the perturbations are introduced (e.g., $\Delta t = 30$ min; 55–85 min for T50 and 95–125 min for T90), T90 shows much greater sensitivity, especially during the early period (see Fig. 8a). Because T90 starts with a supercell storm that has more vigorous dynamics and complex physical processes than T50, the w sensitivity shows a much greater rate of increase.

It is somewhat surprising that the moisture perturbation in the subcloud layer, especially in the updraft region (e_3), exerts a smaller influence on w despite the fact that the absolute perturbations are quite large (cf. Fig. 8b to Fig. 8a). The total number of perturbed grid points in the subcloud layer (i.e., $e_3 + e_4$) is about the same as that of e_1 for T50 and about half that for T90. This implies that vertical velocity is more strongly affected by moisture variations inside the storm (or in the ambient environment) than in the subcloud layer. However, since the maximum sensitivities are mostly observed at upper levels, we examine the relative influence of moisture perturbations to w in the lower levels (around 0.2 and 3 km) in the following.

Figure 9 shows the ratio of maximum w sensitivity for levels $k = 3$ ($z = 227$ m; case K3) and $k = 15$ ($z = 2994$ m; case K15) with respect to the e_1 and e_2 perturbations, respectively, to that with respect to the e_3 perturbation. In general, the moisture perturbations above cloud base [both inside (e_1) and outside (e_2) the cloud] exert a larger influence than those below the cloud base (e_3).

It appears that the time variation of these ratios is strongly tied to the storm behavior at given times. Note that, at the perturbation insertion time ($t = 50$ min), there exist three distinct cells for both the w and Q_v fields at middle levels (see Figs. 2b and 7b, respectively), while both fields near surface are distributed in a broad area associated with the surface outflow (see Fig. 7a for Q_v). Our results suggest that, during the early storm stages (i.e., developing and early mature stages), the middle-level w (K15) is significantly affected by the Q_v perturbation above cloud base (e_1 and e_2). Also, the contribution of the Q_v perturbation below cloud base (e_3) to the lower-level w (K3) is not negligible. This implies that, during the early stages, the updraft is enhanced by nearby moisture sources. The in-storm moisture may directly affect the updraft through condensation, while the environmental moisture above cloud base may indirectly affect w via entrainment and turbulent mixing.

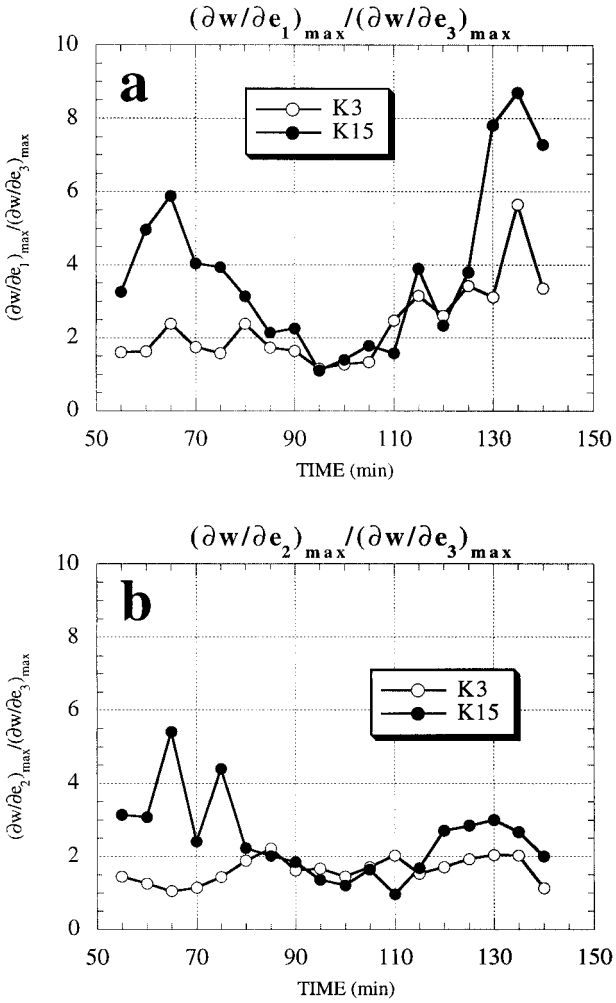

FIG. 9. Ratio between two sensitivity fields at levels of $k = 3$ (case K3; white circle) and $k = 15$ (case K15; black circle): (a) $(\partial w/\partial e_1)_{max}/(\partial w/\partial e_3)_{max}$ and (b) $(\partial w/\partial e_2)_{max}/(\partial w/\partial e_3)_{max}$.

As the major convective cell evolves into a supercell storm around $t = 90$ min (Fig. 2c), the influence of Q_v perturbations on w becomes similar in both K3 and K15. This implies a vigorous transport of subcloud moisture into the storm. After that, as the storm further evolves

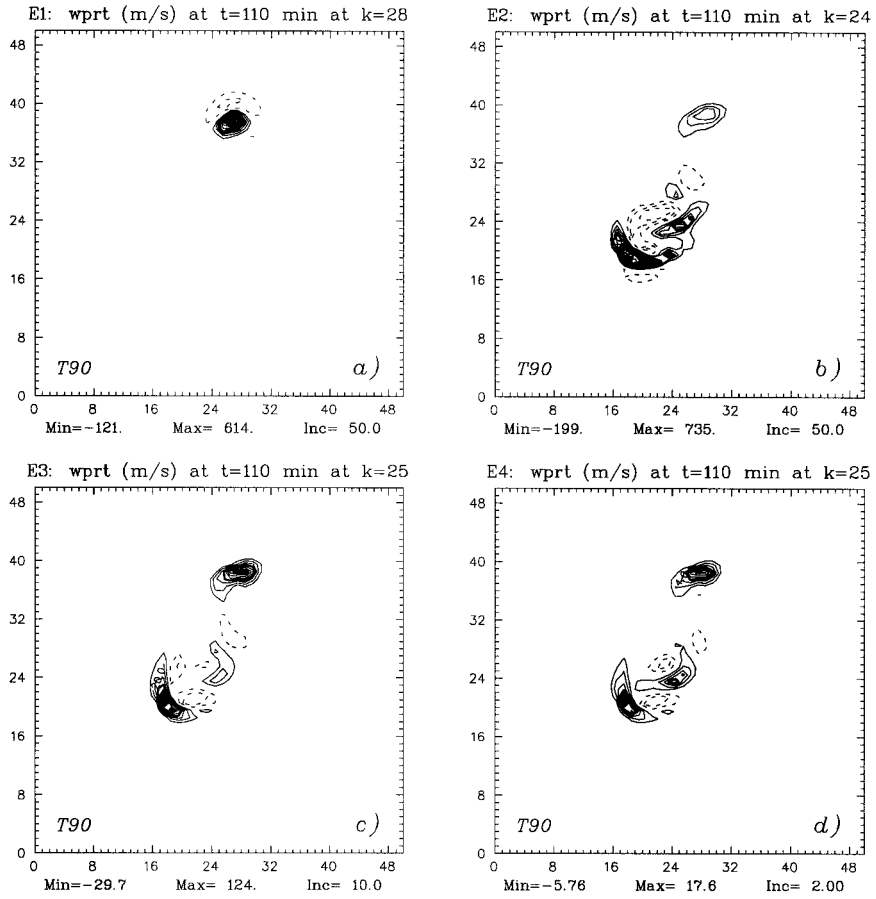

FIG. 10. Domain-maximum sensitivity of w at $t = 110$ min with respect to the water vapor perturbations of (a) e_1, (b) e_2, (c) e_3, and (d) e_4 inserted at $t = 90$ min (in m s^{-1}).

and new cells develop, the influence of the in-storm moisture perturbation (e_1) overwhelms that in subcloud layer (e_3).

We now proceed to investigate the local characteristics of the sensitivity fields for different moisture perturbations. Figure 10 illustrates the general features of w sensitivity for the four perturbations (case T90 at 110 min). The k indices locate the level of maximum w sensitivity. Among all perturbations, the largest sensitivity in w is due to the e_2 perturbation, followed by e_1 (only between 105 and 115 min). It is interesting to note that the locations of the largest sensitivity differ for the four regions perturbed: that for e_1 occurs in the secondary storm near cloud top, while that for e_2 remains near the main storm at lower levels (see Fig. 2d). For perturbations e_3 and e_4, the largest w sensitivity occurs mainly near the main and secondary storms. Similar experiments in a smaller domain by Park and Droegemeier (1996) yielded similar behavior, including the fact that the maximum influence on w of moisture perturbations in the subcloud layer (e_3 and e_4) shifts back and forth between the main and the secondary storms. This appears to be a general tendency at most times.

In order to explain possible mechanisms of the sensitivity results, we have analyzed the air trajectory (not shown) at the perturbation insertion time. They revealed typical behavior that can be observed during a mature stage of convective storms: strong updraft inside the storm that spreads outward at upper levels, downdraft at low levels that spreads out at the surface, and inflow that rides up over the trailing gust front (see Doswell 1985).

When moisture perturbations are added inside the storm (e_1), they can be advected into the environment at upper levels where the saturation vapor pressure is so small that the evaporation of even a small amount of condensed water quickly saturates the air (Emanuel 1994). In addition, an increase of moisture inside the storm brings about intensification of the surface cold pool due to increased updraft intensity and rain production. The stronger convergence at the gust front thus enhances the development of secondary storms.

The amount of moisture in the ambient air, especially far away from the storm, is generally small, and thus the perturbations added (e.g., 10% in e_2) are also small compared to those inside the storm. Thus, they might not be sufficient to affect the secondary storm. However, a large amount of moisture can be found outside the

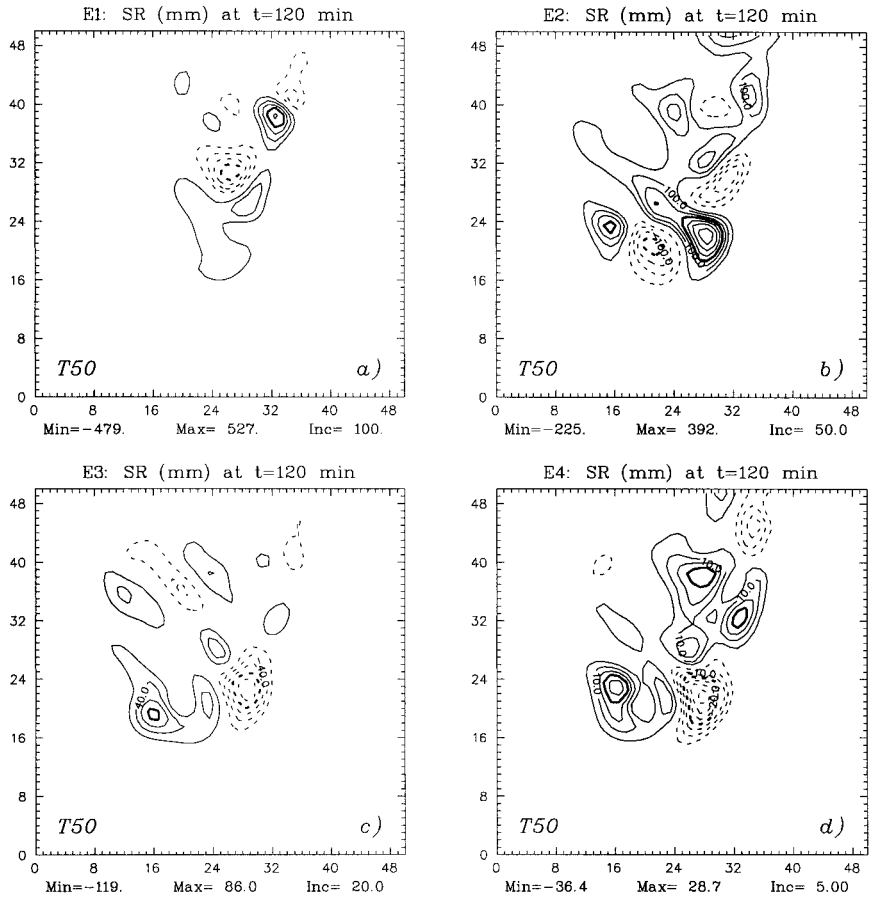

FIG. 11. Sensitivities of surface rainfall at $t = 120$ min with respect to the moisture perturbations of (a) e_1, (b) e_2, (c) e_3, and (d) e_4 at $t = 50$ min (in mm).

storm near the storm boundary. Then an increase in moisture in that area can increase w near the main storm due to an increase in saturation/supersaturations and thus condensation. Also, the added moisture in the ambient air can affect the main storm through mechanisms involving turbulent mixing and entrainment.

In contrast, perturbations added to the updraft region in the subcloud layer (e_3) are transported into the cloud with a residence time depending on the magnitude of updraft. Since the updrafts at lower levels are relatively small, the moisture perturbations may have enough time to affect the main storm through physical processes, including destabilization due to an increase in equivalent potential temperature, an increase of buoyancy, and an increase in cloud water through condensation. It can also affect the secondary storm via the same mechanism in the e_1 perturbation.

In the downdraft region of the subcloud layer (e_4), most moisture perturbations would be advected out with the outflow expansion, then the perturbations add moisture to the environment especially near surface, and thus affect the secondary storm. However, some perturbations that interact with the inflow would go back into the updraft region and could affect the main storm through the same processes as above.

b. *Sensitivity of surface rainfall and accumulated rainfall*

The amount, location, and rate of accumulated precipitation are among the most important quantities in storm-scale prediction. Figure 11 shows the sensitivity of the surface rainfall (SR) at $t = 120$ min with respect to the previous four perturbations inserted at $t = 50$ min (case T50). Recall that at $t = 120$ min, the main updraft is located near the center of the domain as a secondary storm develops to the west (see Fig. 2e). Also, there exists a prominent secondary storm to the northeast of the main storm, along with another weak storm near the northern lateral boundary.

Among all perturbations, the largest sensitivity in SR is due to e_1, that is, water vapor perturbations inside the storm. The major increase in SR occurs in the secondary storm, with a maximum of 527 mm (Fig. 11a). The SR decreases in the weak downdraft region to the north of the main storm with a minimum of -479 mm. This

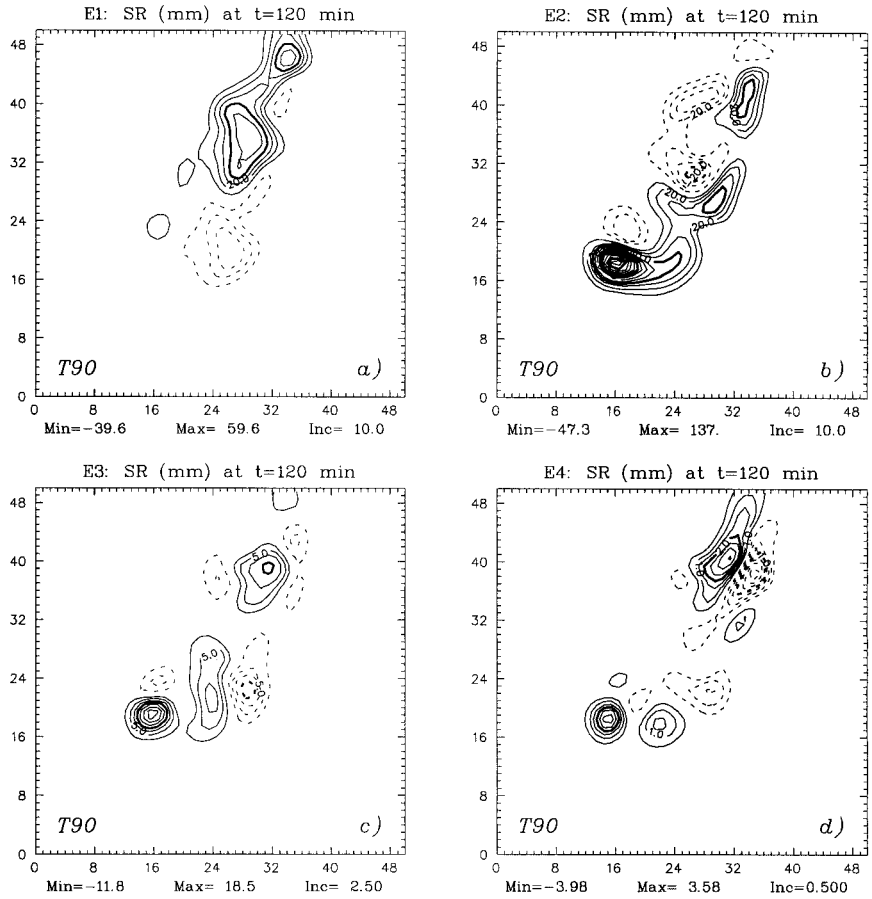

FIG. 12. Same as in Fig. 11 except for the model starting time at $t = 90$ min (in mm).

indicates that a 1% moisture perturbation inside the storm at $t = 50$ min induces a maximum increase of 5.27 mm and a decrease of 4.79 mm in the secondary storm rainfall at $t = 120$ min.

The e_2 perturbation increases SR beneath the main storm (Fig. 11b), while the e_3 and e_4 perturbations result in a decrease in the same area (Figs. 11c and 11d), though the contribution from the e_4 perturbation is quite small.

In Fig. 12, the same sensitivity experiments are portrayed for perturbations inserted at $t = 90$ min (case T90). Note that the verification time is the same as in Fig. 11 (i.e., $t = 120$ min). Possibly due to the relatively shorter sensitivity period, the magnitude of sensitivities is smaller for all perturbations. In contrast to case T50, the largest change in SR among all perturbations in T90 comes from e_2 (Fig. 12b). The major influence area is located to the west of the main storm near the secondary cell.

It is interesting to note that the general feature observed in the *w* sensitivity also applies to the SR for each type of perturbation, at least for the two insertion times considered. That is, the largest influence from the e_1 perturbation tends to be confined to the secondary storm region, while that from e_2 occurs primarily near the main storm. The area of the largest sensitivity due to the e_3 and e_4 perturbations shifts around from storm to storm.

In the context of absolute (dimensional) sensitivity, the SR has smaller sensitivity coefficients to moisture perturbations than *w*. For example, with the same insertion time ($t = 50$ min) and verification time ($t = 120$ min) for a 0.1% e_1 perturbation, *w* increases by a maximum of 6.3 m s^{-1} (see Fig. 8a), while the SR does so by 0.53 mm. However, one should note that each sensitivity has a different dimension and thus should be nondimensionalized to determine relative importance. Computation of the relative sensitivity from Eq. (3) reveals a value of 3.71 for *w* and 61.1 for SR. That is, for a 1% moisture perturbation inside the storm, *w* increases only by 3.71%, while the SR increases by 61.1% at the grid points where the maximum sensitivities are observed. Therefore, *at the location of the maximum sensitivity of each variable*, the surface rainfall is more sensitive to the e_1 perturbation than vertical velocity, in a relative sense.

In Fig. 13 we show the sensitivities of accumulated rainfall (AR) to the same water vapor perturbations de-

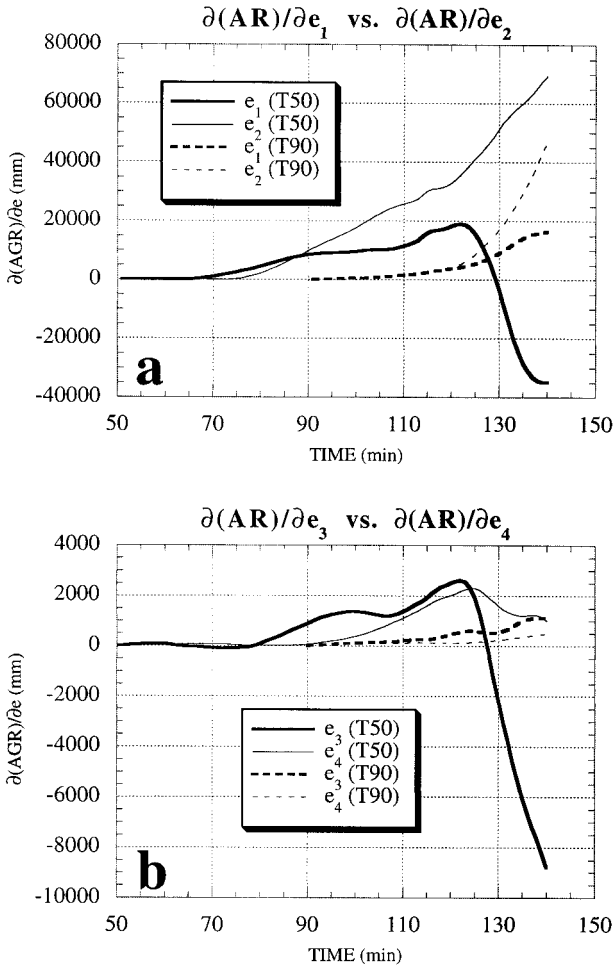

FIG. 13. Same as in Fig. 8 except for sensitivity of accumulated rainfall (in mm).

scribed above. Note that AR is found by integrating the surface rainfall rate in both time and space. On the whole, the largest influence is exerted by moisture perturbations in the ambient environment above cloud base (e_2), followed by those inside the storm (e_1). Both the e_2 and e_4 perturbations induce increases in AR for a given sensitivity period, while the e_1 and e_3 perturbations bring about an increase in AR for most of the period and then decrease after the midlevel updraft of the storm starts to weaken (see Figs. 2c–e).

Note that the e_3 perturbation, which is located in the updraft region below cloud base, is transported into the cloud. The moisture added in this manner serves as a source for more cloud water through condensation, and then for more rainwater through autoconversion and collection. The increased rainwater induces an increase in the terminal velocity and loading and eventually increases the downdraft. As the midlevel updraft weakens, this increased downdraft leads to an earlier decay of the storm. That is, the moisture perturbation inside the storm increases the surface rainfall while the storm is still vigorous; however, it eventually induces an earlier decay of the storm and thus a decrease in the accumulated rainfall.

An increase in moisture in the ambient environment does not have a strong and direct impact on the dynamics inside the storm. Though it lessens the effects of turbulent entrainment, the overall impact of the perturbations may not be as significant as for e_1 and e_3. The e_2 perturbation exerts an influence inside the storm in a steady and slow manner. On the other hand, it can provide an opportunity for new clouds to form in the ambient air where the moisture is added and thus increase the rainfall.

If one believes that the typical magnitude of water vapor observational errors is a few percent, then the increase in AR during the sensitivity period is not significant compared to the magnitude of AR in the control run. For example, the largest change in AR (which occurs at 140 min, caused by the e_2 perturbation) is only 349 mm for a 1% perturbation, which is only about 1.1% of the AR at that time. When the expected vapor error is quite large, however, one may expect a considerably larger change in AR, especially over long periods of time.

These results suggest that inaccuracies in the observation or retrieval of the water vapor field may, in storm-scale predictions, lead to considerable errors in the numerical solution after only a short period of time. The changes so induced are likely to be more significant in instantaneous fields, such as vertical velocity, compared to time-integrated fields, such as accumulated rainfall.

7. Implications for variational data assimilation and forecast error

Having examined the sensitivity of model solutions with respect to water vapor perturbations, we now use the SE-ARPS to compute sensitivity of a functional, which measures the square distance between observations and a numerical forecast (often referred to as the cost function), with respect to perturbations in all model variables and to interpret the sensitivity results in the context of four-dimensional variational data assimilation and forecast error. In 4D-Var, one seeks to minimize the cost function over some period of time (the data assimilation period) and to optimize the initial guess fields in selected model inputs [see Zou and Navon (1994) for a review on the theory]. Most minimization algorithms require the gradient of the cost function with respect to specified control variables (e.g., initial conditions) in order to determine the optimal direction of decent [e.g., Lewis and Derber (1985); Wang et al. (1997); Park and Droegemeier (1997b)—see Zou et al. (1993b) for a review on large-scale unconstraint minimization algorithms]. This gradient information is usually provided by backward integration of adjoint models, though more recently, a method has been developed that does not

require gradient information and minimization algorithm (Kalnay et al. 1999).

Using subjectively chosen initial guess fields, sensitivity analysis can reveal which variables in the initial guess fields have a significant influence on the model solution. Conversely, the same information can indicate the extent to which variables can be altered to yield identical changes in the solution (Meyers et al. 1994). Using results from sensitivity analysis, Wang et al. (1992) identified input parameters that exert large impact on the change in cost function.

When applied to 4D-Var, sensitivity information, especially derivatives of the cost function with respect to all initial fields, can indicate the alterations in the initial field that are required to change the cost function by a specific amount on the way to its minimum state. One can quantify the relative importance of the initial guess fields in 4D-Var using the RSC [see Eq. (3)], which is normalized by its NLM control run counterpart (Sykes et al. 1985; Meyers et al. 1994; Park and Droegemeier 1999).

The accuracy of the assimilated fields and the time required for reaching the minimum of the cost function are highly related to the shape of the cost function (Chao and Chang 1992). This shape is determined by the relative contribution of each term, including the model forecast, observational fields, and weight functions [e.g., see Eq. (5)] as well as the nonlinearity associated with the assimilation period and the error characteristics. This implies that, for a variable having a relatively large impact, even a small change in that variable may affect the shape of the cost function significantly.

Here we examine the relative sensitivities of a specified cost function with respect to all initial states in the 3D ARPS. Using the approach described in section 2, we investigate sensitivities in two regions: 1) points for which $Q_r > 1.0 \times 10^{-4}$ g g^{-1} and 2) the remaining ambient environment. By doing so, we seek to gain insight into how 4D-Var can be improved via the availability of sensitivity information. Although the quality (i.e., accuracy and performance) of variational data assimilation is dependent upon many factors such as the choice of minimization algorithm, the way that the cost function is defined, choice of weighting function, quality of scaling and preconditioning, etc. [see Zou and Navon (1994) for the basic framework of variational data assimilation], we confine our discussion here only on the relative importance of observation/retrieval errors among all model variables.

a. Cost function

We define the cost function (J) as the weighted sum of squared distance between the model state ($\mathbf{X}$) and available observations ($\mathbf{X}^\circ$) distributed in space and time:

$$J = \sum_{n=1}^{N} \langle \mathbf{W}_\mathbf{X}(\mathbf{X}_n - \mathbf{X}_n^o), (\mathbf{X}_n - \mathbf{X}_n^o)\rangle, \qquad (5)$$

where $\langle \mathbf{A}, \mathbf{B}\rangle$ denotes an inner product between $\mathbf{A}$ and $\mathbf{B}$, and n represents the time index. The weighting matrix, $\mathbf{W}_\mathbf{X}$, is computed following Wang (1993). The weight function of any variable is defined to be inversely proportional to its forecast error, which is summed from the perturbation insertion time to the verification time (Wang 1993). In this manner, the cost function is nondimensionalized and becomes unity at the beginning of the variational data assimilation.

b. Pseudo-observations

We consider the control simulations from section 4 (see Fig. 2) as our pseudo-observations. The sensitivity period is 30 min, extending from $t = 80$ min to $t = 110$ min. A 1% perturbation is added to all variables at all grid points at 80 min for the perturbation run, which serves as the nonlinear basic field for the sensitivity computation. At both 90 and 110 min, the perturbation run shows development of the secondary storm to the north of the main storm (cf. Figs. 14a and 14b to Figs. 2c and 2d, respectively). Otherwise, the two runs are very similar.

Note that the ARPS predicts the perturbations of θ and p. Since the total fields of θ and p are observed (or retrieved) in practice (i.e., base state + perturbation), we specify their total fields as independent variables for the sensitivity computation.

c. Sensitivity of cost function

In Table 2, we show the sensitivities of the cost function (J) to perturbations in specified variables inside the storm. Because the gradients are nondimensional, we can compare their relative importance at any given time. To compare the relative importance *among times*, however, we need to normalize the sensitivity by its corresponding cost function from the nonlinear model.

The largest sensitivity in the cost function (i.e., forecast error) occurs as a result of errors in potential temperature (θ), followed by pressure (p) and water vapor (Q_v). The sensitivities are positive for all three perturbations. At the time of error insertion ($t = 80$ min), the influence of p on J is much larger than that of θ. After about 10 min, the influence of θ starts to exceed that of p. On the whole, the cloud water (Q_c) perturbation exerts the smallest influence on the cost function.

The pressure is directly related to the mass balance through pressure gradient forces in the momentum equations. When the pressure is perturbed, the flow will accelerate until terms involving the velocity become comparable with pressure gradient force. Therefore, the flow will immediately and significantly respond to the pressure perturbations. In contrast, perturbations in potential temperature affect the system initially through the buoy-

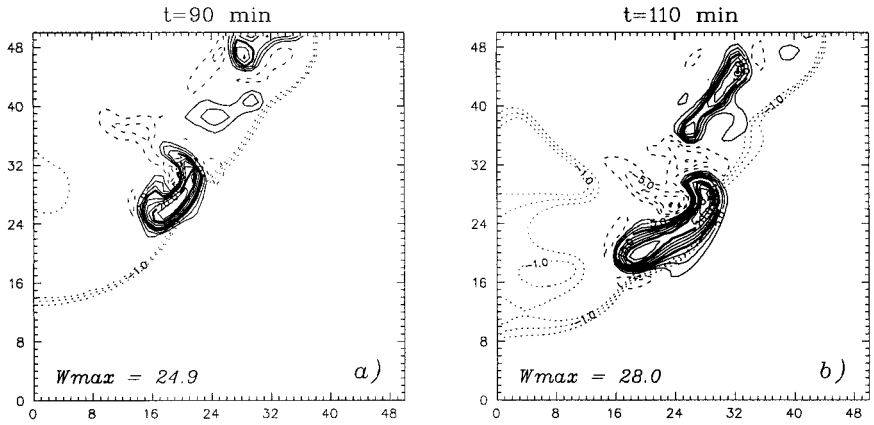

FIG. 14. Same as in Fig. 2 except for a perturbed run with a 1% perturbation in all fields inside the storm at $t = 80$ min at (a) 90 and (b) 110 min.

ancy term in the vertical momentum equation. That is, whereas the pressure affects all three components of velocity simultaneously through pressure gradient force, the potential temperature affects only the vertical velocity initially and then other variables through mass continuity. Hence, during the early sensitivity period, pressure perturbations exert the largest influence on forecast errors among all variables. However, the increased buoyancy resulting from temperature perturbations eventually influences storm dynamics and forecast error.

Among the moisture variables inside the storm, water vapor exerts the largest influence on J, followed by rainwater (Q_r) and cloud water. An increase in Q_v increases the equivalent potential temperature and thus destabilizes the atmosphere, which enhances convective motion. It also affects the amount of liquid water through condensation and latent heating. Hence, Q_v affects momentum, and thermodynamic and moisture variables through indirect physical processes. The Q_r perturbation influences the downdraft through loading, and thermodynamic and moisture variables via evaporation. The Q_c perturbation initially affects only the thermodynamic and moisture variables through evaporation, autoconversion, and accretion.

Perturbations in the momentum variables (u, v, and w) inside the storm yield small changes in J. Among them, the largest sensitivity of J is due to the v perturbation and the smallest is due to the u perturbation.

In storm scale, the most common way to obtain in-storm observation is using Doppler radars, which provide information on radial velocity and reflectivity. Thus most model variables should be retrieved. Our results suggest that the cost function is more sensitive to errors in retrieving temperature and pressure fields than others. As suggested by Wang et al. (1992), the results also imply that the inaccuracy of retrieving these quantities inside the storm has more impact on the quality of 4D-Var.

Table 3 depicts the sensitivities of J with respect to perturbations of model variables in the ambient environment at 80 min. Overall, the sensitivities are smaller than those for perturbations inside the cloud, except for the u field. Note the prominent decrease in the influence of perturbations in p on J (compare with Table 2). Although the p perturbation still induces the largest effect at the error insertion time, its influence diminishes afterward compared to other variables. Since Q_c and Q_r are effectively zero in the environment, the sensitivities of J to them are extremely small.

In the ambient environment, the thermodynamic and moisture fields are only vertically stratified. Thus, the horizontal pressure gradient force is negligible. However, perturbations in θ and Q_v give an impact on all variables in a manner similar to the in-storm perturbations. The largest sensitivity in the cost function is due to θ, followed by Q_v and p. This implies that the cost function is strongly affected by perturbations in

TABLE 2. Sensitivity of cost function at a given time with respect to the perturbations of model variables inside the cloud at 80 min.

t (min)	$\partial J/\partial e_u$	$\partial J/\partial e_v$	$\partial J/\partial e_w$	$\partial J/\partial e_\theta$	$\partial J/\partial e_p$	$\partial J/\partial e_{Q_v}$	$\partial J/\partial e_{Q_c}$	$\partial J/\partial e_{5Q_c}$
80	0.0015	0.001	0.001	8.0	24.47	0.02	0.001	0.003
85	0.0001	−0.006	0.022	14.3	24.48	0.16	−0.003	−0.02
90	−0.0114	−0.023	0.030	26.3	24.50	0.47	−0.007	−0.06
95	−0.0263	−0.055	0.037	45.1	24.59	0.97	−0.013	−0.10
100	−0.0212	−0.102	0.042	68.9	24.75	1.66	−0.017	−0.15
105	0.0001	−0.177	0.044	100.5	25.02	2.60	−0.018	−0.21
110	0.0069	−0.281	0.043	143.4	25.47	3.78	−0.013	−0.32

TABLE 3. Same as in Table 2 except for perturbations in an ambient environment.

t (min)	$\partial J/\partial e_u$	$\partial J/\partial e_v$	$\partial J/\partial e_w$	$\partial J/\partial e_\theta$	$\partial J/\partial e_p$	$\partial J/\partial e_{Q_v}$	$\partial J/\partial e_{Q_c}$	$\partial J/\partial e_{Q_r}$
80	$-0.7e^{-11}$	$0.6e^{-11}$	$0.2e^{-12}$	$0.3e^{-7}$	$0.2e^{-6}$	$0.9e^{-9}$	$-0.1e^{-11}$	$-0.1e^{-15}$
85	0.001	0.002	0.0006	−1.7	−0.05	$0.5e^{-6}$	−0.0004	$0.6e^{-7}$
90	−0.01	0.008	−0.001	−4.4	−0.07	−0.04	−0.0006	$-0.3e^{-6}$
95	−0.06	0.023	−0.003	−11.0	−0.12	−0.18	−0.0011	−0.0001
100	−0.19	0.059	−0.005	−24.2	−0.17	−0.77	−0.0013	−0.0002
105	−0.42	0.134	−0.006	−50.8	−0.30	−2.24	−0.0017	−0.0005
110	−0.68	0.188	−0.003	−107.7	−0.74	−4.63	0.0008	−0.0011

environmental temperature and water vapor fields and thus the accuracy of observations of such quantities is also essential for the quality of 4D-Var.

Overall, perturbations in observed/retrieved potential temperature, pressure, and water vapor fields have more impact on the cost function than those in the other fields. With this kind of sensitivity, however, it is difficult to compare the time evolution of a given variable, in a relative sense. To accomplish this, we need to normalize the sensitivity through Eq. (3). Note that the sensitivity is already nondimensionalized through the weight functions. Since the weight function is designed to make the cost function unity at the verification time, the sensitivities at 110 min are automatically normalized.

In Fig. 15, we show the time evolution of the relative sensitivities of J [i.e., $(\partial J/\partial e)/(J/e)$] with respect to perturbations in θ and p (i.e., e_θ and e_p) inside the cloud at 80 min. Note that the sensitivity of J to the p perturbation increases very slowly with time (see Table 2). However, the RSC of J shows a maximum at the error insertion time and then rapidly decreases toward the verification time. This implies that pressure perturbation has a significant influence on forecast error only during the period immediately after the errors are inserted, largely through adjustments via the creation of acoustic modes. In contrast, the RSC of J with respect to the θ perturbation increases logarithmically with time.

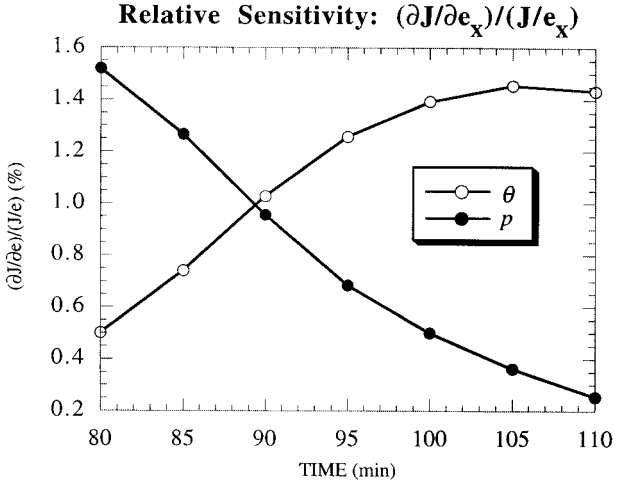

FIG. 15. Relative sensitivities of cost function with respect to the perturbations in potential temperature (white circle) and pressure (black circle) inside the storm at $t = 80$ min.

It is noteworthy that the RSC of J to the θ perturbation exceeds that to the p perturbation about 10 min after the errors are inserted. This suggests that, in the context of data assimilation, the changes in p at the beginning of the assimilation period result in larger changes in the cost function than that at the end of the assimilation period, and vice versa for θ. It also implies that, for a very short assimilation period (e.g., 5 min), the quality of 4D-Var is more dependent upon the accuracy of p than that of θ, and vice versa for a longer assimilation period (e.g., >10 min).

The quality of 4D-Var is also affected by the choice of the assimilation period (Luong et al. 1998). However, choosing an optimal assimilation period is a complicated issue. In the 4D-Var experiment with the moist ARPS, Park and Droegemeier (1997b) showed that a shorter assimilation period does not necessarily produce better results. As indicated by Luong et al. (1998), an inadequately short assimilation period may not allow the information of assimilated data to spread into the whole model domain. On the other hand, an inadequately long assimilation period may lead to a cost function that has multiple minima and thus convergence to a local minimum (Li 1991).

This type of sensitivity analysis is useful for determining the appropriate starting point of assimilation, if the magnitude of observation/retrieval errors is known for each variables. For example, when relative errors in θ are larger than those in p, we might consider choosing the starting point of assimilation much earlier than the end of assimilation period (110 min in our case), that is, a longer assimilation period, so that errors in θ do not affect the cost function strongly. This is true in general because temperature responds to velocity at a slower pace and thus a longer period is needed for temperature to obtain appropriate information from the velocity fields. However, one should avoid choosing an inadequately long assimilation period for the reason explained above.

Our results also indicate that temperature perturbations have a greater impact than pressure on forecast error over a long time period. Thus, we desire that our initial conditions have less error in temperature than in pressure (and any other variables).

The RSCs of J for perturbations in other variables inside the storm (Table 2 at $t = 110$ min) indicate that the sensitivities to u, Q_c, and w are almost negligible.

Similar analyses with perturbations in the ambient environment reveal that the J sensitivity is almost negligible to w, Q_c, and Q_r. This suggests that, in the context of variational data assimilation and forecast error, the accuracy requirement for observation/retrieval of these variables is less strict than that of other variables that exert great impact on the cost function (i.e., θ, p, and Q_v).

8. Summary and discussion

In this paper we applied an automatic differentiation tool (ADIFOR) to investigate first the validity of the tangent linear approximation in a moist convective storm simulated using the 3D ARPS model. Then we examined the sensitivity of model outputs with respect to perturbations in water vapor in various regions and stages of the storm. Finally, we computed the sensitivities of the cost function to perturbations of all model variables to assess the relative importance of observation/retrieval errors on four-dimensional variational data assimilation and forecast error.

For the deep convective storm studied here, the tangent linear model solutions, which describe the evolution of perturbations along trajectories of a time-dependent nonlinear base state, represent the corresponding nonlinear perturbation fields accurately up to 50–80 min for a 1% moisture perturbation over the entire model domain. For a 10% perturbation, which is a magnitude similar to observational errors, the TLM is valid for 10–30 min.

Considering the highly nonlinear and discontinuous properties of solutions in a full-physics nonhydrostatic cloud model such as ARPS, these results should prove useful for future studies of storm predictability, data assimilation, and Doppler radar retrieval, all of which require derivative or sensitivity information. We also note that ADIFOR has no problem in generating the derivative code of a compressible model with a mode-splitting time integration scheme.

In agreement with other studies, mostly of the Observing System Simulation Experiment type, we found that bias-type errors in the water vapor field exert various modes of influence on storm evolution. When inserted inside the storm, the perturbations mostly influence the development of new storms. The effect of perturbations in the ambient environment is confined largely to the main storm with only weak effects on secondary storms. Perturbations placed in the subcloud layer affect both the main and secondary storms, depending upon the time of insertion. This effect may be limited only to the storm considered here, and the mechanisms responsible for this behavior are not yet understood.

Moisture perturbations inserted in the storm exert the largest influence on storm features such as vertical velocity and surface rainfall, followed by perturbations in the ambient environment. The accumulated rainfall showed the largest sensitivity to environmental moisture perturbations. Although perturbations in the subcloud layer have a smaller effect on upper-level storm dynamics, they do affect the low-level dynamics, especially during the early sensitivity period.

It is apparent that the evolution of individual storms, and thus their predictability using a numerical model, is strongly influenced by errors in the vapor field, though the specific impact depends upon the location (in time and space) and probably the type of error considered. The strong sensitivity of vertical velocity to in-storm and environmental vapor perturbations implies that accurate observations or retrievals of this field are likely required for accurate storm predictions. The same accuracy is also plausibly necessary for the vapor field in subcloud layer for the accurate prediction of low-level features.

But how accurate is accurate? What accuracy is required in observed water vapor to have a reasonably good storm prediction using a numerical model? Sensitivity information does not necessarily give a direct answer to this question. First, one needs to establish criteria for the accuracy of a forecast. One also needs to determine the importance of forecast error in a specific variable at a specific time and location or variables integrated over time and space (i.e., cost function). Once the criteria for an acceptable forecast error are determined, one can easily evaluate the accuracy requirement for observational data through relative sensitivity analysis.

We have demonstrated that both the absolute and relative sensitivity analyses provide valuable information on the response of the cost function (i.e., forecast error) to changes in various control parameters (here the model initial states). Unfortunately, these techniques reveal only the effect and not the cause. The perturbations inside the storm generally exerted a greater impact on forecast error than those in ambient environment. At the verification time, the largest sensitivity in the cost function was due to θ, followed by p and Q_v for in-storm perturbations, and due to θ, followed by Q_v and p, for perturbations in the environment. This implies that the inaccuracy in observing or retrieving these fields (especially θ) has a strong impact on the quality of the variational data assimilation.

We also note that, at least for our case, the p field has the largest effect on forecast error immediately after the errors are inserted, while the θ field does so over a longer period. This implies that, for a very short assimilation period, the quality of 4D-Var is more dependent upon the accuracy of p than that of θ, and vice versa for a longer assimilation period. However, the assimilation period should be determined carefully because an inadequately short or long assimilation period exerts harmful impacts on the quality of 4D-Var.

This type of sensitivity analysis also has implications for predictability. In the context of predictability, the sensitivity information identifies, for the same change

in each variable, which variable may induce a larger forecast error at some specific time. Although this sensitivity information does not include nonlinear effects, it does provide the fundamental characteristics of the changes in solution behavior and forecast error, which might be very useful for designing appropriate experiments.

Acknowledgments. We are grateful to Drs. Chris Bischof and Gordon Pusch at Argonne National Laboratory and Dr. Alan Carle at Rice University for their assistance in applying ADIFOR to ARPS. We also acknowledge Dr. John Lewis at the National Severe Storms Laboratory for valuable discussions on variational data assimilation. This research represents a portion of the first author's doctoral dissertation and was supported by the National Science Foundation under Grant ATM92-22576 to the second author and by Grant ATM91-20009 to the Center for Analysis and Prediction of Storms, University of Oklahoma. The computer simulations were performed on the Cray J90 at the Environmental Computing Application System (ECAS), University of Oklahoma. ECAS is supported by the NSF under Grant EAR95-12145, with additional support provided by American Airlines.

REFERENCES

Arakawa, A., and V. R. Lamb, 1977: Computational design of the basic dynamical processes of the UCLA general circulation model. *Methods in Computational Physics,* Vol. 17, *General Circulation Models of the Atmosphere,* J. Chang, Ed., Academic Press, 174–265.

Bischof, C., and F. Dilley, 1995: A compilation of automatic differentiation tools. *ACM SIGNUM Newsl.,* **30,** 2–20.

——, A. Carle, P. Khademi, and A. Mauer, 1996a: ADIFOR 2.0: Automatic differentiation of Fortran 77 programs. *IEEE Comput. Sci. Eng.,* **3,** 18–32.

——, G. D. Pusch, and R. Knoesel, 1996b: Sensitivity analysis of the MM5 weather model using automatic differentiation. *Comput. Phys.* **10,** 605–612.

Chao, W. C., and L.-P. Chang, 1992: Development of a four-dimensional variational analysis system using the adjoint method at GLA. Part I: Dynamics. *Mon. Wea. Rev.,* **120,** 1661–1673.

Crook, N. A., 1996: Sensitivity of convection initiation to low-level thermodynamics fields. *Mon. Wea. Rev.,* **124,** 1767–1785.

Doswell, C. A., III, 1985: The operational meteorology of convective weather. Volume II: Stormscale analysis. NOAA Tech. Memo. ERL ESG-15, 240 pp. [Available from U.S. Government Printing Office, Washington, DC 20402.]

Droegemeier, K. K., S. M. Lazarus, and R. Davies-Jones, 1993: The influence of helicity on numerically simulated convective storms. *Mon. Wea. Rev.,* **121,** 2005–2029.

——, and Coauthors, 1996: Realtime numerical prediction of storm-scale weather during VORTEX '95. Part I: Goals and methodology. Preprints, *18th Conf. on Severe Local Storms,* San Francisco, CA, Amer. Meteor. Soc., 6–10.

Dunker, A. M., 1981: Efficient calculation of sensitivity coefficients for complex atmospheric models. *Atmos. Environ.,* **15,** 1155–1161.

Elliot, W. P., and D. J. Gaffen, 1991: On the utility of radiosonde humidity archives for climate studies. *Bull. Amer. Meteor. Soc.,* **72,** 1507–1520.

Emanuel, K. A., 1994: *Atmospheric Convection.* Oxford University Press, 580 pp.

Errico, R. M., and T. Vukicevic, 1992: Sensitivity analysis using an adjoint of the PSU–NCAR Mesoscale Model. *Mon. Wea. Rev.,* **120,** 1644–1660.

Giering, R., 1997: Tangent linear and adjoint model compiler, users manual, version 1.0. TAMC version 4.7. Tech. Rep. Max-Planck-Institut für Meteorologie, 44 pp.

Gilmore, M. S., and L. J. Wicker, 1996: The influence of DCAPE on supercell dynamics. Preprints, *18th Conf. on Severe Local Storms,* San Francisco, CA, Amer. Meteor. Soc., 723–727.

Hong, X., M. Leach, and S. Raman, 1995: A sensitivity study of convective cloud formation by vegetation forcing with different atmospheric conditions. *J. Appl. Meteor.,* **34,** 2008–2028.

Kalnay, E., S. K. Park, Z.-X. Pu, and J. Gao, 2000: Application of the quasi-inverse method to data assimilation. *Mon. Wea. Rev.,* in press.

Kessler, E., 1969: *On the Distribution and Continuity of Water Substance in Atmospheric Circulations. Meteor. Monogr.,* No. 32, Amer. Meteor. Soc., 84 pp.

Klemp, J. B., and R. B. Wilhelmson, 1978: The simulation of three-dimensional convective storm dynamics. *J. Atmos. Sci.,* **35,** 1070–1096.

Krumm, W. R., 1954: On the cause of downdrafts from dry thunderstorms over the plateau area of the United States. *Bull. Amer. Meteor. Soc.,* **35,** 122–125.

Leith, C. E., 1974: Theoretical skill of Monte Carlo forecasts. *Mon. Wea. Rev.,* **102,** 409–418.

Lewis, J. M., and J. C. Derber, 1985: The use of adjoint equations to solve a variational adjustment problem with advective constraints. *Tellus,* **37A,** 309–322.

Li, Y., 1991: A note on the uniqueness problem of variational adjustment approach to four-dimensional data assimilation. *J. Meteor. Soc. Japan,* **69,** 581–585.

Luong, B., J. Blum, and J. Verron, 1998: A variational method for the resolution of a data assimilation problem in oceanography. *Inverse Probl.,* **14,** 979–997.

Meyers, S. D., C. S. Jones, D. M. Legler, K. F. Miles, and J. J. O'Brien, 1994: The sensitivity to parametric variation in direct minimization techniques. *Mon. Wea. Rev.,* **122,** 1632–1639.

Park, S. K., and K. K. Droegemeier, 1996: Adjoint sensitivity analysis of a 3-D convective storm. Preprints, *18th Conf. on Severe Local Storms,* San Francisco, CA, Amer. Meteor. Soc., 235–239.

——, and ——, 1997a: Validity of the tangent linear approximation in a moist convective cloud model. *Mon. Wea. Rev.,* **125,** 3320–3340.

——, and ——, 1997b: 4DVAR with a moist adjoint applied to deep convective storms—Simulated data experiments. Preprints, *Second US–Korea Joint Workshop for Storm- and Mesoscale Weather Analysis and Prediction,* Seoul, Korea, KOSEF/NSF/CAPS/KMA/KMS, 52–56.

——, and ——, 1999: Sensitivity analysis of a moist 1D Eulerian cloud model using automatic differentiation. *Mon. Wea. Rev.,* **127,** 2180–2196.

——, ——, and C. Bischof, 1996: Automatic differentiation as a tool for sensitivity analysis of a convective storm in a 3-D cloud model. *Computational Differentiation: Techniques, Applications, and Tools,* M. Berz et al., Eds., SIAM, 205–214.

Pratt, R. W., 1985: Review of radiosonde humidity and temperature errors. *J. Atmos. Oceanic Technol.,* **2,** 404–407.

Ronen, Y., 1988: Uncertainty analysis based on sensitivity analysis. *Uncertainty Analysis,* Y. Ronen, Ed., CRC Press, 41–70.

Rostaing, N., S. Dalmas, and A. Galligo, 1993: Automatic differentiation in Odyssée. *Tellus,* **45A,** 527–535.

Seigneur, C., T. W. Tesche, P. M. Roth, and L. E. Reid, 1981: Sensitivity of a complex urban air quality model to input data. *J. Appl. Meteor.,* **20,** 1020–1040.

Shine, K. P., and A. Sinha, 1991: Sensitivity of the earth's climate to height-dependent changes in the water vapor mixing ratio. *Nature,* **354,** 382–384.

Sykes, J. F., J. L. Wilson, and R. W. Andrews, 1985: Sensitivity analysis for steady state groundwater flow using adjoint operators. *Water Resour. Res.*, **21,** 359–371.

Wang, Z., 1993: Variational data assimilation with 2-D shallow water equations and 3-D FSU global spectral models. Ph.D. thesis, The Florida State University, 235 pp. [Available from Department of Mathematics, The Florida State University, Tallahassee, FL 32306.]

——, I. M. Navon, F. X. Le Dimet, and X. Zou, 1992: The second order adjoint analysis: Theory and applications. *Meteor. Atmos. Phys.*, **50,** 3–20.

——, K. K. Droegemeier, M. Xue, and S. K. Park, 1995: Sensitivity analysis of a 3-D compressible storm-scale model to input parameters. *Second International Symposium on Assimilation of Observations in Meteorology and Oceanography*, Vol. II, WMO/TD-No. 651, 437–442.

——, ——, L. White, and I. M. Navon, 1997: Application of a new adjoint Newton algorithm to the 3D ARPS storm-scale model using simulated data. *Mon. Wea. Rev.*, **125,** 2460–2478.

Weygandt, S. S., K. K. Droegemeier, C. E. Hane, and C. L. Ziegler, 1990: Data assimilation experiments using a two-dimensional cloud model. Preprints, *16th Conf. on Severe Local Storms*, Kananaskis Park, AB, Canada, Amer. Meteor. Soc., 493–498.

Worley, B. A., E. M. Oblow, F. G. Pin, R. E. Maerker, J. E. Horwedel, R. Q. Wright, and J. L. Lucius, 1987: Deterministic methods for sensitivity and uncertainty analysis in large-scale computer models. *Proceedings of a Conference on Geostatistical, Sensitivity, and Uncertainty Methods for Ground-Water Flow and Radionuclide Transport Modeling*, B.E. Buxton, Ed., Battelle Press, 135–154.

Xue, M., K. K. Droegemeier, V. Wong, A. Shapiro, and K. Brewster, 1995: ARPS 4.0 user's guide. CAPS, 380 pp. [Available from Center for Analysis and Prediction of Storms, University of Oklahoma, Norman, OK 73069.]

——, and Coauthors, 1996: Real time numerical prediction of storm-scale weather during VORTEX-95. Part II: Operation summary and example cases. Preprints, *18th Conf. on Severe Local Storms*, San Francisco, CA, Amer. Meteor. Soc., 178–182.

Zou, X., and I. M. Navon, 1994: Variational data assimilation: Some aspects of theory and application. *Environmental Modeling*, Vol II, *Computer Methods and Software for Simulating Environmental Pollution and its Adverse Effects*, P. Zannetti, Ed., Computational Mechanics Publications, 277–323.

——, A. Barcilon, I. M. Navon, J. Whitaker, and D. G. Cacuci, 1993a: An adjoint sensitivity study of blocking in a two-layer isentropic model. *Mon. Wea. Rev.*, **121,** 2833–2857.

——, ——, M. Berger, P. K. H. Phua, T. Schlick, and F.-X. Le Dimet, 1993b: Numerical experience with limited-memory quasi-Newton and truncated-Newton methods. *SIAM J. Optim.*, **3** 582–608.

——, I. M. Navon, and J. G. Sela, 1993c: Variational data assimilation with moist threshold processes using the NMC spectral model. *Tellus*, **45A,** 370–387.